Stabilized Phase Transition Process of Layered NaxCoO2 via Ca-Substitution

Hasegawa, Hirona ; Ishado, Yuji ; Okada, Shigeto ; Mizuhata, Minoru ; Maki, Hideshi ; Matsui, Masaki

(Citation)
Journal of The Electrochemical Society,168(1):010509-010509

(Issue Date)
2021-01-01

(Resource Type)
journal article

(Version)
Version of Record

Journal of The Electrochemical
Society

The Electrochemical Society
Advancing solid state & electrochemical science & technology

Stabilized Phase Transition Process of Layered Na_xCoO_2 via Ca-Substitution

To cite this article: Hirona Hasegawa *et al* 2021 *J. Electrochem. Soc.* **168** 010509

Journal of The Electrochemical Society, 2021 **168** 010509

Stabilized Phase Transition Process of Layered Na_xCoO_2 via Ca-Substitution

Hirona Hasegawa,[1] Yuji Ishado,[2] Shigeto Okada,[2,3] Minoru Mizuhata,[1] Hideshi Maki,[1] and Masaki Matsui[1,3,*,z]

[1]*Department of Chemical Science and Engineering, Kobe University Rokkodai-cho, Nada, Kobe, Hyogo 657-8501, Japan*
[2]*Institute for Materials Chemistry and Engineering, Kyushu University, Kasuga-koen, Kasuga 816-8580, Japan*
[3]*Elements Strategy Initiative for Catalyst and Batteries (ESICB), Kyoto University, Japan*

We investigated the suppressed capacity fading of a Ca-substituted P3-type Na_xCoO_2 during the charge/discharge process. The Ca-substituted Na_xCoO_2 shows similar phase transition behavior to the Ca free one, with an expanded P′3 phase region. The capacity fading of the Na_xCoO_2 is highly correlated with the phase transition at 4.0 V of P′3–O3′ phase transition and at 2.7 V of O′3–P′3 phase transition. The amount of Co_3O_4 observed in the cycled electrodes corresponds to the capacity loss during the cycling test. Thus, the migration of the $Co^{3+/4+}$ ions during the phase transition process causes the capacity fading. The decomposition of the electrolyte solution also accelerates the migration of the $Co^{3+/4+}$ ions. Though the Ca-substitution does not prevent the phase transition, the Ca-substituted Na_xCoO_2 shows improved capacity retention.

Manuscript submitted October 12, 2020; revised manuscript received December 5, 2020. Published January 7, 2021.

Supplementary material for this article is available online

Lithium-ion batteries are mostly utilized for portable electronic devices such as smartphones, laptops, and tablets. The demand for lithium-ion batteries for automotive applications has been increasing due to the expansion of electric vehicles and renewable energy storage applications. However, since lithium resources are limited, alternative energy storage systems have been widely explored in recent years. The sodium-ion batteries are expected to be promising candidates for post lithium-ion batteries because of material abundance.

Layered sodium transition metal oxides Na_xTMO_2 ($x \leqq 1$, TM = Transition metal) have been widely studied as candidates for the cathode active materials of sodium-ion batteries.[1] They show complex phase transition behaviors associated with the gliding of the TMO_2 slabs during the insertion/desertion of Na^+ ions. The variety of the phases, which the layered transition metal oxides take, are classified into O3, P3, O2, P2, etc., according to the stacking sequence of the oxygen close–packed layer.[2] Also, the phase transition behavior is dependent upon the choice of the transition metal species.[3–10]

O3-type NaFeO2 shows a phase transition from the hexagonal O3 structure to the monoclinic O′3 structure associated with the desertion of Na^+ ions during the charging process. At the end of the O3–O′3 biphasic region, the Fe^{3+} ions easily migrate to face-shared tetrahedral sites in sodium layers from the O′3 structure. As a consequence, the electrochemical inactive Fe_3O_4 is formed.[3,4] In contrast, O3-type $NaCoO_2$ shows relatively good reversibility with various complicated phase transitions, such as O3-O′3-P′3 and P3 phases.[5,6]

The elemental substitution of the transition metal is a popular material design strategy for improving the reversibility of the layered Na_xTMO_2. Yoshida et al. reported a cobalt-substituted O3-type $NaFe_{1-x}Co_xO_2$ showed a large reversible capacity and good rate capability compared with $NaFeO_2$.[11] P2-type $Na_{2/3}Fe_{1/2}Mn_{1/2}O_2$ shows improvement in reversibility at high cell voltage by Fe-substitution.[12] Various combinations of the transition metals were investigated to obtain high-capacity layered cathode active materials with improved energy density and cyclability.[11–15]

Elemental substitution of Na sites is not a straightforward strategy of the battery materials design because the substituted element hinders the diffusion of the carrier ions. However, several research groups reported the Ca-substitution of the layered Na_xTMO_2 as an alternative approach for the improved electrochemical performances.[16–20] Ca-doped P2-type Na_xCoO_2 shows a stable cycling performance. However, the Ca-substitution decreases the capacity and increases the overpotential as a series of trade-offs.[16,17] We recently reported that the Ca-substitution of a P′3-type Na_xCoO_2 improves the cycling performance without increasing the overpotential. The DFT calculation results show that the activation energy of the phase transition from the O3 to the O1 phase is increased by Ca substitution. The results indicate that the substituted Ca^{2+} ions inhibit the irreversible O3–O1 phase transition.[18] Unfortunately, since the O1 phase is not detected even at 4.5 V, the correlation between the phase transition and the cycling performance is still unclear. In addition, further investigation is necessary to understand the role of the Ca^{2+} ions to maintain the cycling performance.

In the present study, we investigate the phase stability of the P3-type layered Na_xCoO_2 with/without Ca-substitution using XRD. Then, we conduct a series of cycling tests under various voltage ranges to clarify the correlation between the phase transition and cycling performance. We also performed DFT calculations to discuss the Ca-substitution effect on the phase transition corresponding with the degradation mode of the layered Na_xTMO_2 layered cathodes.

Experimental

Synthesis and characterization.—The Na_xCoO_2 and $Na_xCa_yCoO_2$ were synthesized by conventional solid-state reactions using a stoichiometric amount of sodium hydroxide (NaOH, Wako) and cobalt hydroxides ($Co(OH)_2$, Kojundo Chemical Laboratory) and calcium hydroxide ($Ca(OH)_2$, Wako) as starting materials. The excess NaOH of 15 wt.% was added to compensate for the evaporation of sodium during the calcination process. The starting materials were thoroughly mixed using an agate mortar and pestle in an argon-filled glove box. The mixed precursors are pelletized and calcined at 500 °C for 36 h under O_2 flow.

Structural characterization of the Na_xCoO_2 and $Na_xCa_yCoO_2$ were performed using an X-ray diffractometer (D8 Advance, Bruker) equipped with Co-Kα radiation. All the measurements were carried out using an airtight sample holder to avoid air exposure. The structural refinement is performed using RIETAN-FP.[21] The surface

*Electrochemical Society Member.
[z]E-mail: matsui@godzilla.kobe-u.ac.jp

morphologies were observed using FE-SEM (JSM-6335F, JEOL) and the elemental mapping was taken by EDX (JED-2200, JEOL). Surface analyses of the cycled electrode were performed using an FTIR spectrometer (NicoletTM iS50, Thermo Fisher Scientific), equipped with a diamond ATR accessory (Golden GateTM, Specac).

Electrochemical measurements.—The electrochemical properties of the Na_xCoO_2 and $Na_xCa_yCoO_2$ were studied using two-electrode cells (TJ-AC, Tomcell JAPAN). The composite electrodes were prepared by mixing 80:10:10 weight ratio of the active material, acetylene black (SuperP®, Imerys), and PVdF-HFP (KYNAR®, ARKEMA) dissolved in anhydrous N-Methyl-2-pyrrolidone (NMP, Sigma-Aldrich) for the preparation of the electrode slurry. The slurry was coated on an aluminum current collector and vacuum dried at 120 °C for 1.5 h. The dried electrode was punched into a circular disc of 16 mm diameter. The punched electrode was pressed at 20 MPa and dried at 120 °C for 3 h under vacuum. The obtained electrode was coupled with a sodium metal (Nakalai Tesque) electrode to prepare a half-cell. The electrolyte solution was 1 mol l^{-1} of $NaPF_6$ dissolved in ethylene carbonate (EC) and methyl carbonate (DMC) mixed solvent in a 1:1 ratio by volume, containing fluoroethylene carbonate (FEC) of 3 wt% as an electrolyte additive (Kishida Chemical).

The galvanostatic charge-discharge tests were performed using a battery charger (TOSCAT-3100, Toyo System) at room temperature. Formation cycles were performed in the voltage range of 2.0–4.0 V at a rate of 6.4 mAg^{-1}. Cycling tests were performed during various voltage ranges at 1C rate, which was defined based on the last discharged capacity of formation cycles.

Theoretical calculations.—Density functional theory (DFT) calculations were performed with the projector augmented wave (PAW) approach, which is implemented in the Vienna Ab initio Simulation Package (VASP).[22,23] The optB86b-vdW functional was used to account for the Van der Waals interaction between CoO_2 layers. Hubbard U correction was not applied, since +U correction can lead to incorrect results for Na_xCoO_2.[24] The cutoff energy was set to 520 eV. A gamma-centered k-point for which the density is more than 500/(number of atoms) was adopted.

The migration barriers for Ca^{2+} ions in P3-$Na_xCa_yCoO_2$ were calculated by the Climbing Image Nudged Elastic Band (CI-NEB) method, which is implemented in VASP Transition State Theory (VTST) tools as an extension of VASP code.[25,26] In the NEB calculations, a 3 × 6 × 1 supercell (36 formula units) was used for the P3-type structure so that the hopping Na^+ and Ca^{2+} ions achieved a sufficient distance between their periodic images. The force is converged within 0.02 eV $Å^{-1}$.

Results and Discussion

Figure 1 shows the X-ray diffraction patterns of $Na_xCa_yCoO_2$ ($y = 0, 0.02, 0.04, 0.06$). Regardless of the Ca content, all the diffraction patterns are attributed to the P′3-type $Na_{0.81}CoO_2$ (NCO) with the space group of *C 2/m*. Figure S1 (available online at stacks.iop.org/JES/168/010509/mmedia) shows a Rietveld refinement result and the SEM-EDX images of $Na_{0.69}Ca_{0.04}CoO_2$ (NCCO). The structural refinement result proves the Ca^{2+} ions partially replace the Na^+ ions at the *8j* sites. We consider the Ca-substitution occurs at the Na site due to the similar ionic radii of the Na^+ ion and the Ca^{2+} ion. The SEM-EDX results confirm that the calcium is uniformly distributed in the particles.

Next, we discuss the phase transition behavior of NCO and NCCO during the insertion/desertion process of Na^+ ions. Ex situ XRD patterns of NCO and NCCO electrodes with voltage profiles are shown in Fig. 2. The NCO shows an O3 single phase after the discharging process at 2.0 V. On the other hand, the NCCO has two phases of O3 and O′3 phase due to the Na-vacancies formation by the substituted Ca^{2+} ions. Then both the NCO and NCCO electrodes show the O′3 phase at 2.6 V. The results show the O3–O′3 phase transition occurs at the initial plateau around 2.55 V. The NCO has O′3 and P′3 binary phases at the 2nd plateau region of 2.7 V, while the NCCO shows a P′3 single phase. The result indicates the phase transition from O′3 to P′3 completes at a slightly lower electrode potential of 2.7 V due to the Ca-substitution.

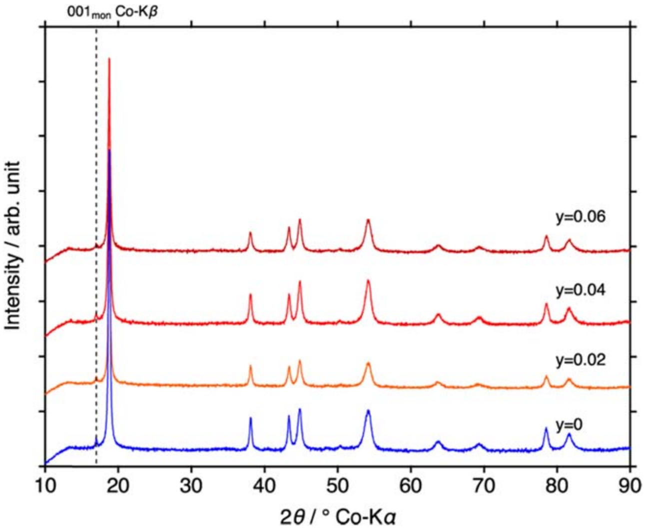

Figure 1. Powder XRD patterns of $Na_xCa_yCoO_2$ ($y = 0, 0.02, 0.04, 0.06$). All the diffraction patterns are assigned to the monoclinic P′3 phase with the space group of *C 2/m*.

Subsequently, a wide P′3 single phase region appears at 2.8 or 2.7 to 3.9 V. The Na content of NCO and NCCO in this region is $0.71 > x > 0.42$ and $0.70 > x > 0.38$, respectively. In both cases, the 001 peak of the P′3 phase shifts to a lower angle during the charging process suggesting the interlayer distance expands upon the Na-extraction. Once NCO and NCCO are charged up to 4.0 V, Na^+ ion content: x reaches to 0.36 and 0.34, respectively. This desertion of Na^+ ions causes phase transition from P′3 to O3′ single phase via the two-phase region. The series of phase transition behaviors from O′3 to P′3 at the low electrode potential is generally consistent with those of O3-type $NaCoO_2$.[5,6]

On the other hand, the phase transition at the high potential does not match the convex hull calculated in our previous paper. The convex hull shows that NCCO has P′3–O3′ binary region at 4.0 V, while O3′ single phase is observed, as shown in Fig. 2d. Considering DFT calculations estimate the formation of O3′ phase at high potential, the results are in qualitative agreement with the theoretical calculations. We need to characterize more deeply to explain this point. In other regions, the phase transition behavior of NCO and NCCO is almost the same. Therefore, the phase transition of NCO is not actually suppressed in the present Ca content of NCCO. In other words, the glide of the CoO_2 layer of Ca-substituted NCO is relatively easy to occur.

We have performed DFT calculations to understand the Ca substitution effect on the phase transition behavior. Figure 3a shows the activation energies of the P′3 to O′3 phase transition processes for $Na_{0.333}CoO_2$ and $Na_{0.278}Ca_{0.056}CoO_2$. The activation energy of the phase transition from P′3 to O3′-type NCO via a transition state is approximately 10 meV, while the NCCO shows the activation energy of 20 meV. Even though the calculation results suggest that the Ca-substitution hinders the phase transition from P′3-type to O3′-type (and vice versa), the activation energy of the phase transition of NCO is much lower than the migration barrier of the Na^+ ions in the layered structure: 300 meV. Therefore, the Ca-substitution does not prevent the series of phase transitions, as discussed in the previous section.

We also calculated the migration barrier of a Ca^{2+} ion in the layered structure. The migration paths of Na^+ ion and Ca^{2+} ion in P3-$Na_{0.278}Ca_{0.056}CoO_2$ are shown in Figs 3c and 3d. The migration

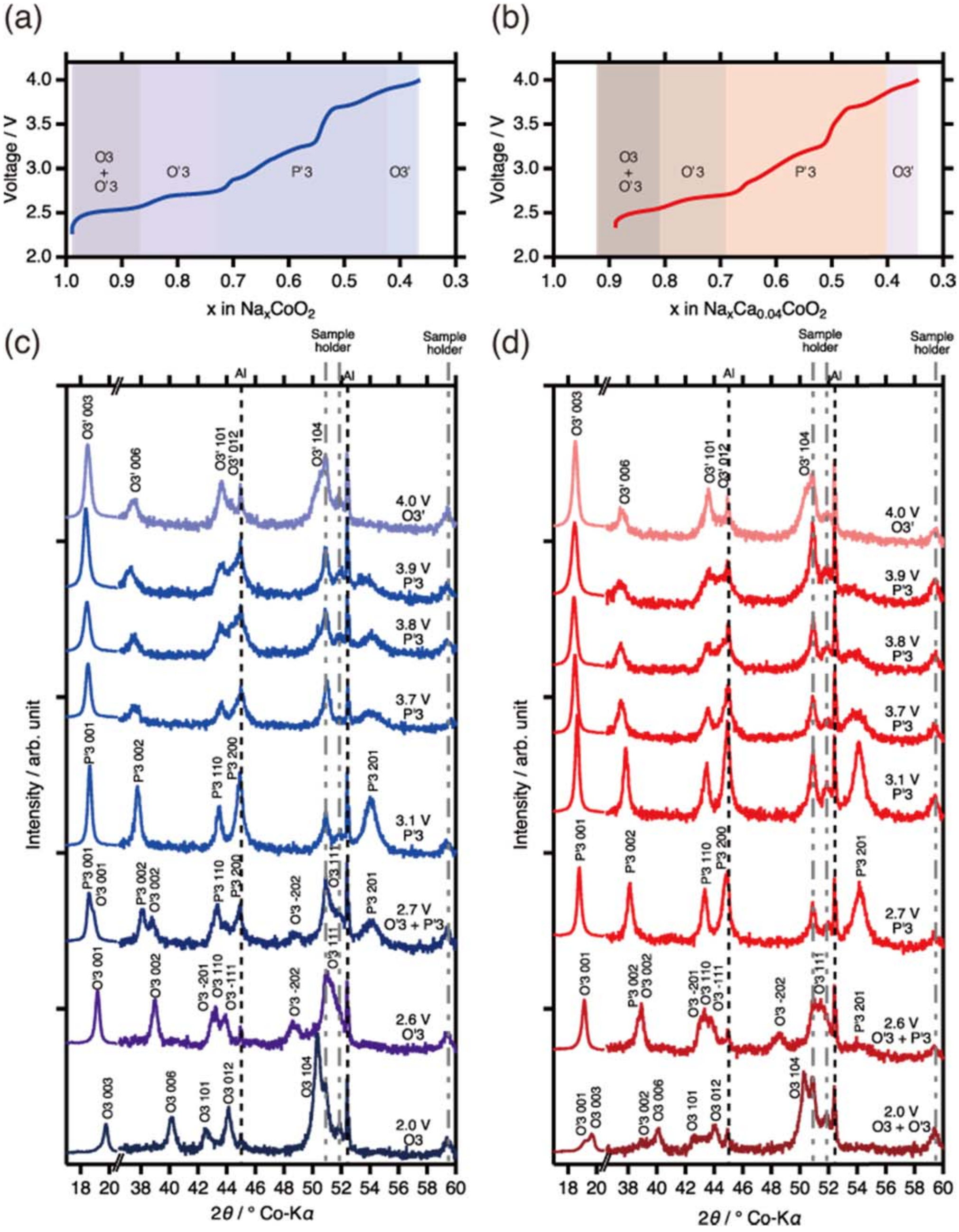

Figure 2. Galvanostatic charge curve (up to 4.0 V at 6.4 mAg^{-1}) for Na$_{0.81}$CoO$_2$ (a) and Na$_{0.69}$Ca$_{0.04}$CoO$_2$ (b) electrodes. Ex situ XRD patterns of Na$_{0.81}$CoO$_2$ (c) and Na$_{0.69}$Ca$_{0.04}$CoO$_2$ (d) during the second charging process.

barrier for the Ca^{2+} ion is 509 meV, almost double the Na^{+} ion reported in the previous paper. The difference in the migration barrier of Na^{+} ion and Ca^{2+} ion corresponds to the four-digit differences in the diffusion coefficient.[27] Hence the long-range diffusion of Ca^{2+} ions during the charging/discharging process is almost negligible. However, in the case of short-range migration between the face-sharing prismatic sites, the migration barrier of the Ca^{2+} ion shows a relatively low value of 350 meV. We assume the short-range migration of the Ca^{2+} ions enable the Na^{+} ion ordering, which is observed in the phase transition process upon Na intercalation/deintercalation. Consequently, the NCCO exhibits a similar phase transition behavior as NCO during the charging/discharging process. On the other hand, the relatively easy movement of Ca^{2+} ions remind the extraction of Ca^{2+} ions from the NCCO during cycling. Figure S2 shows a series of EDX mapping for an NCCO electrode after 200 cycles. The uniform distribution of Ca shows that the Ca^{2+} ions remain in the layered structure.

We also investigated how the phase transition behavior affects the capacity retention. The phase stability of the NCO and NCCO at each electrode potential shown in Fig. 2 is similar to each other. Hence, we conducted a series of cycling tests at various voltage ranges to control each phase transition process.

First, we performed cycling tests in the voltage range of 2.0–4.0 V, including all the phase transitions: O3 to O′3 at 2.55 V, O′3 to P′3 at 2.7 V, and P′3 to O3′ at 4.0 V discussed above. We can ignore the influence of the P′3–O3′ phase transition by cycling the cell at 2.0–3.7 V. Furthermore, the cycling test conducted in the voltage range of 2.8–3.7 V provides the capacity retention of the NCO in the P′3 single phase region without any phase transition. We ignore a series of phase transitions from P′3–P3–P′3 phase, observed around

3.0 V because the phase transitions occur in a very narrow voltage range. Therefore, we consider the voltage range of 2.8–3.7 V as P′3 single phase region.

Figures 4a and 4b show the cycling performances of NCO and NCCO for 200 cycles operated at the various voltage ranges. In the voltage range of 2.0–4.0 V, the initial discharging capacity of NCO is 120 $mAhg^{-1}$. Significant capacity fading is observed in the following cycles. The discharged capacity at 50th and 100th cycle decreases to 55% and 21% of the initial discharged capacity, respectively. The cell retains only 6.4% of the initial discharged capacity after 200 cycles. On the other hand, the NCCO delivers 109 $mAhg^{-1}$ at the 1st cycle. Despite the low capacity of NCCO at the 1st cycle, the cyclability is remarkably improved compared with NCO. The capacity retention of the NCCO is 85% at 50th cycle, 77% at 100th cycle. The NCCO retains 58% of the 1st discharging capacity after 200 cycles.

The NCO half-cell cycled in 2.0–3.7 V shows improvement in capacity retention by avoiding the P′3–O3′ phase transition around 4.0 V. The NCO at the 50th cycle maintains the discharge capacity of 75 $mAhg^{-1}$: 83% of the initial cycle. Even with the improved cycling performance, the NCO still shows capacity decay during cycling. The capacity retention of the NCO at the 100th and 200th cycle is 65% and 36%, respectively. The continuous capacity decay suggests that another phase transition at low electrode potential also leads to capacity loss. On the other hand, the NCCO shows further improvement in the capacity retention of 83% even at the 200th cycle. The excellent cycling performance of the NCCO suggests that the Ca-substitution also improves the reversibility of the O′3–P′3 phase transition at low electrode potential. The NCO also shows further improvement in cycling performance by limiting the operation voltage range of 2.8–3.7 V corresponding to the P′3 single phase region. The capacity retention of the NCO cycled at 2.8–3.7 V is 84% even after 200 cycles.

The above results show that the series of phase transitions during the charging/discharging process lead the capacity loss in case of NCO. We found both the O′3–P′3 transition at low electrode potential and the P′3–O3′ transitions at high electrode potential lead to the capacity fading. The stable cycling performance in the P′3 single-phase region also proves the strong correlation between the phase transition and the capacity loss. The results also suggest that the Ca-substitution improves the reversibility of the phase transition process.

To identify the trace of the irreversible phase transition, we performed XRD measurements of the cycled electrodes. The XRD patterns of the cycled NCO and NCCO electrodes are shown in Fig. 5. Since the electrodes are charged up to 3.1 V after the cycling test, all the electrodes have the P′3 phase as the main component of

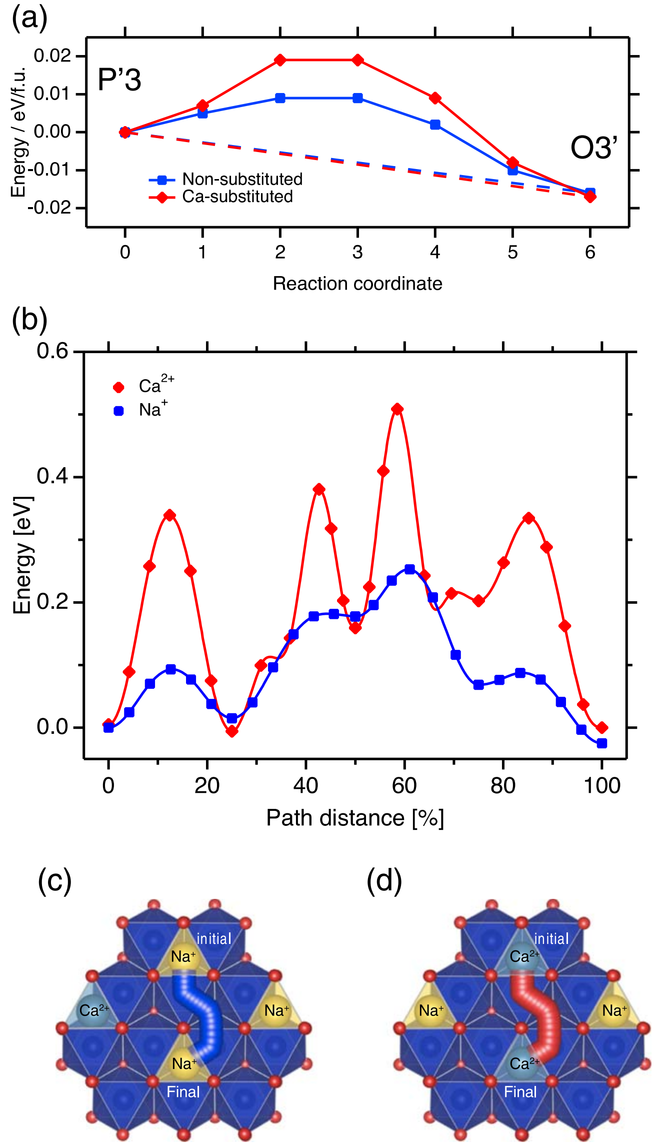

Figure 3. Activation energy for the P′3–O3′ phase transition of $Na_{0.333}CoO_2$ and $Na_{0.278}Ca_{0.056}CoO_2$ (a) and migration barrier for the Ca^{2+} ions and Na^{+} ions in P3-$Na_{0.278}Ca_{0.056}CoO_2$. (b). The migration paths of Na^{+} ions (c) and Ca^{2+} ions (d) used in the DFT-NEB calculation.

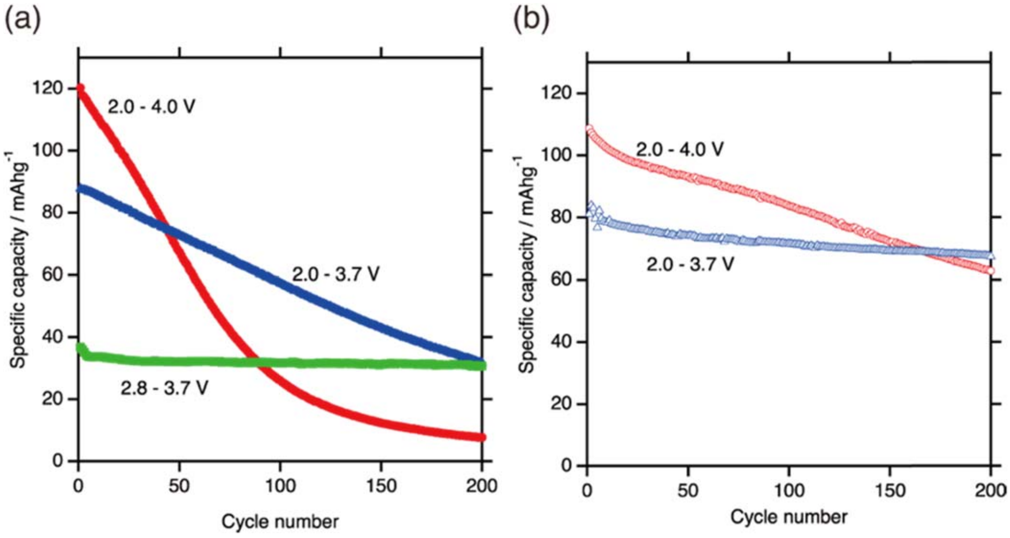

Figure 4. Cycling performances of the NCO (a) and NCCO (b) cycled at various voltage ranges.

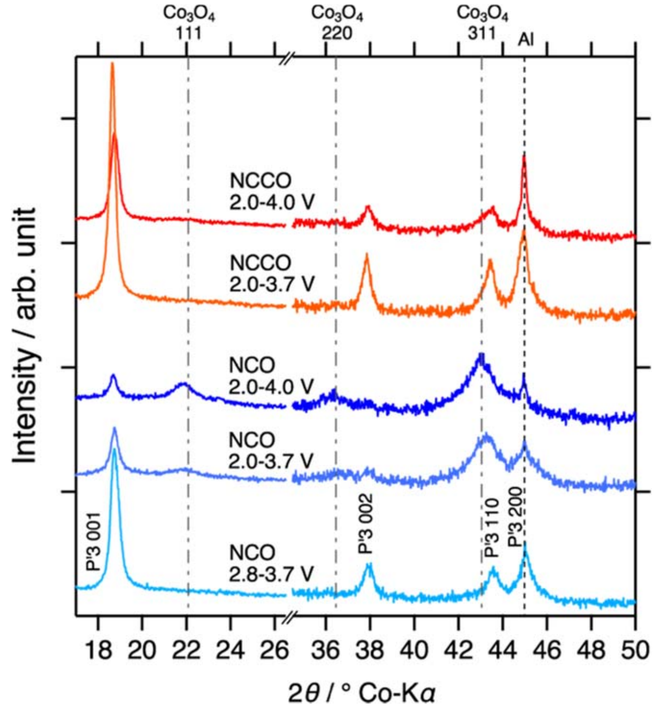

Figure 5. XRD patterns of the NCO and NCCO electrodes after the cycling test.

the active material. The XRD pattern of the NCO electrode cycled at 2.0–4.0 V has two broad peaks at 21.9 ° and 36.5 °, attributed to the 111 and 220 reflections of Co_3O_4. Moreover, the peak intensities of the P′3 phase are relatively low. Formation of the Co_3O_4 suggests the phase separation of NCO to Co_3O_4 leads the capacity fading during the cycling test.

The NCO electrodes cycled in the voltage range of 2.0–3.7 V also has the Co_3O_4. The low intensity of the peaks corresponding to Co_3O_4 reflects the less formation of Co_3O_4. In the present case, the amount of Co_3O_4 also reflects the specific capacity loss during the cycling test. We believe that the phase transition during the charge/discharge process causes the phase separation of the NCO because the NCO cycled in the voltage range of 2.8–3.7 V has no Co_3O_4. The trend is also consistent in the case of the NCCO. A small amount of Co_3O_4 is detected in the electrode cycled in the voltage range of 2.0−4.0 V. On the other hand, the Co_3O_4 almost disappeared in the NCCO cycled at 2.0−3.7 V. The improved capacity retention by the Ca-substitution directly reflects the amount of the Co_3O_4.

Even though it is difficult to make a quantitative discussion based on the above XRD results, it is obvious that the capacity retention of layered NCO highly correlates with the Co_3O_4 formation during the phase transition. The effect of the Ca-substitution is also consistent with the trend. The Ca substitution suppresses the formation of the Co_3O_4 rather than inhibiting the phase transition itself.

Here we propose a possible Co_3O_4 formation process from NCO during the phase transition. The formation of Co_3O_4 with spinel structure from the layered Na_xCoO_2 requires the migration of the $Co^{3+/4+}$ ions into the sodium layer. In the case of the P′3–O3′ phase transition around 4.0 V, the Na^+ ion content x in the Na_xCoO_2 is around 0.4. Many Na vacancies available in the Na layer enable the $Co^{3+/4+}$ ions to migrate into the Na layer easily. An example of the formation process of the Co_3O_4 from NCO can be described in the following Eq. 1.

$$Na_{0.5}CoO_2 \rightarrow 2/3Na_{0.75}CoO_2 + 1/9Co_3O_4 + 2/9O \qquad [1]$$

Note that the oxidation state of cobalt ions in the $Na_{0.75}CoO_2$ and Co_3O_4 is lower than in $Na_{0.5}CoO_2$. Hence the extra oxygen atoms need to be consumed as shown in the equation. The extra oxygen atoms need to be consumed via some side reaction to compensate for the charge balance. Since the P′3–O3′ transition occurs around a high electrode potential of 4.0 V vs Na, the preferable reaction in the present system is the oxidation of the electrolyte component such as solvent molecules and anion species. Figure 6 shows a schematic representation of the possible Co_3O_4 formation process via oxidation of an ethylene carbonate molecule. The reduction and migration of the $Co^{3+/4+}$ ions simultaneously occur associated with the oxidation of the electrolyte solution.

The O′3–P′3 phase transition at 2.7 V also forms Co_3O_4 during the cycling. In this case, Na vacancies available for the migrated cobalt ions are limited; thus, the Co_3O_4 formation probability becomes lower than the phase transition at 4.0 V.

We also presume that the Co_3O_4 formation is unlikely to occur in the P′3 phase because the NaO_6 prismatic site in the P′3 phase is too large for the cobalt ions. Therefore, the NCO electrode cycled in the voltage range of 2.8–3.7 V shows the excellent capacity retention without the Co_3O_4 formation. Considering the XRD study in Fig. 5, the substituted Ca^{2+} ions hinder the $Co^{3+/4+}$ ions from migrating into the Na layer in the NCCO. We suppose that the electrostatic

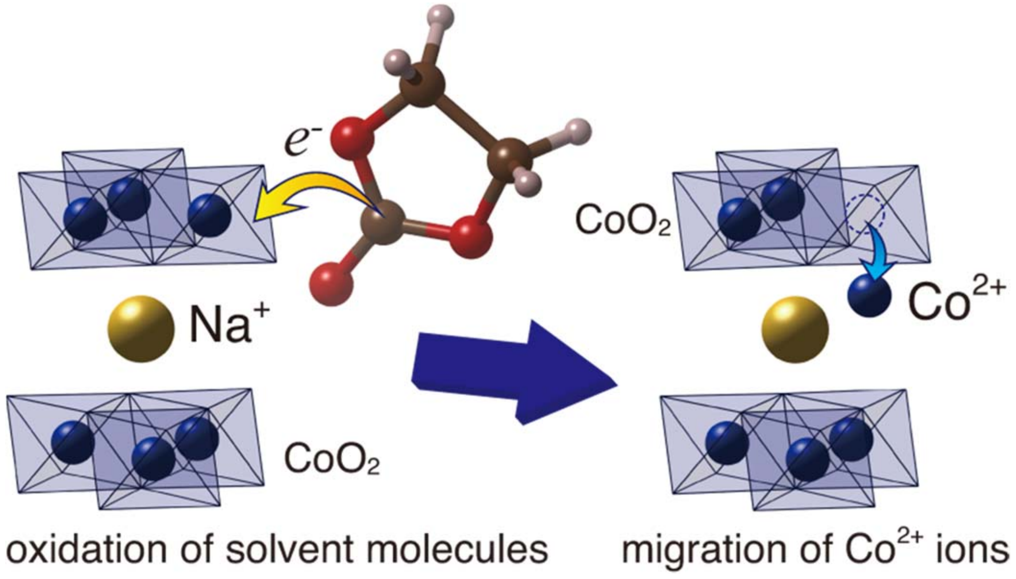

Figure 6. Schematic representative of the proposed degradation process of Na_xCoO_2.

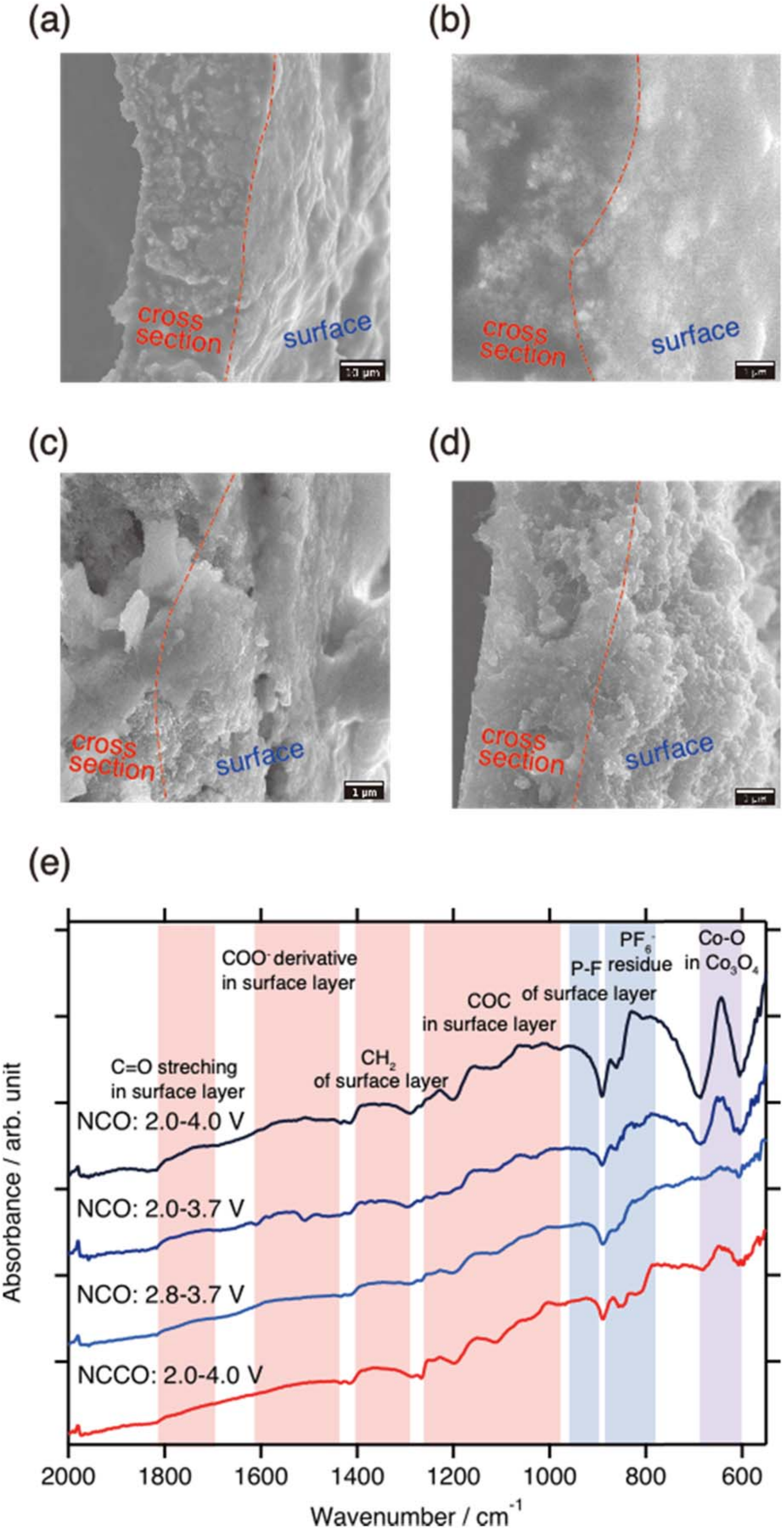

Figure 7. SEM images of the NCO (a), (b), NCCO (c) electrodes cycled in the voltage range of 2.0–4.4 V, compared with an as-prepared NCCO (d). ATR-FTIR spectra for the NCO electrodes cycled in the various voltage ranges of 2.0–4.0 V, 2.0–3.7 V and 2.8–3.7 V, compared with the NCCO electrode cycled in 2.0–4.0 V (e).

repulsion between Ca^{2+} ion and $Co^{3+/4+}$ ions prevents the cobalt ions migration into the Na layers. Figure S3 shows possible structures of the NCCO after the cobalt ion migration with the energy gap: ΔE by the cobalt ion migration. The relatively large ΔE lead by the cobalt ion at the neighboring site of the Ca^{2+} site indicates that the calcium ions hinder the cobalt ions migration.

The Co_3O_4 formation process at the high electrode potential proposed in the previous section reminds us that the decomposed products of the electrolyte solution are supposed to form a surface layer. Here we attempt to identify the decomposed products at the surface of the electrode. Figures 7a–7d are the cross-section view of NCO and NCCO electrodes. The surface morphology of the cycled NCO electrode obviously has a thick surface layer as shown in Fig. 7a. We suspect the decomposed products are also accumulated inside the composite electrode, because the magnified image is blurred as shown in Fig. 7b. The NCCO electrode also has a surface layer, as shown in Fig. 7c. Though the NCCO electrode is also covered with the decomposed products, particle shape is still clearly observed in the cross-section image. Since the surface morphologies of the particles are similar to the as-prepared electrode shown in Fig. 7d, the electric conductivity of the cycled NCCO electrode is well maintained.

ATR-FTIR measurements for the cycled NCO and NCCO electrodes were carried out to characterize the surface layer, as shown in Fig. 7e. The FTIR spectrum of the NCO electrode cycled in 2.0–4.0 V has a strong peak around 640 cm^{-1} corresponds to the Co–O stretching vibration of Co_3O_4, suggesting that the NCO particles are mostly decomposed into the Co_3O_4, and the result is consistent with the XRD results shown in Fig. 5. The overall trend of the Co-O stretching vibration peak is also in good agreement with the XRD. The NCO in 2.0–3.7 V and the NCCO in 2.0–4.0 V show relatively weak peak at 640 cm^{-1}, while the peak intensity of the NCO cycled in 2.8–3.7 V is negligible.

A series of peaks at 750–850 cm^{-1} are assigned to the anion derivatives. The peaks observed at 825 cm^{-1} and 870 cm^{-1} are assigned to the P–F stretching vibration mode of the decomposed products or residue of PF_6^- anion. Also, the broad peak around 770 cm^{-1} corresponds to NaF. Series of broad peaks observed at 1006, 1145, 1230 and 1350 cm^{-1} are corresponding to C–O–C stretching vibration mode of decomposed EC or DMC. Also, the vibration modes of the decomposed anion such as PO_2^-, PO_3^{2-} and PO_4^{3-} are observed at 1000–1300 cm^{-1} region. The broad peaks observed within the 1300–1400 cm^{-1} region suggest CH_2 wagging vibration peaks of decomposition of EC and DMC. The weak broad peaks observed within 1400–1800 cm^{-1} correspond to the C=O and COO^- stretching vibration peaks of decomposed EC and DMC such as carboxylic and ester derivatives. These peaks observed on the NCO electrode cycled in 2.0–4.0 V are slightly stronger than other electrodes, indicating that the Co_3O_4 formation is associated with the decomposition of the electrolyte solution.

Conclusions

In the present study, we investigated the correlation between the phase transition and the capacity fading of the layered Na_xCoO_2. Ex situ XRD study revealed that both the NCO and NCCO show similar phase transition behavior during the charge/discharge process. DFT calculation results suggest that the increased activation barrier of the P′3-O3′ phase transition by Ca-substitution is negligible. The capacity retention of NCO is significantly lower than NCCO cycled in the voltage ranges of 2.0–4.0 V, as we reported previously. In this voltage region, the NCO and NCCO typically show phase transition processes during the charging process at a low electrode potential of 2.7 V vs Na and a high electrode potential of 4.0 V vs Na. The capacity retention of the NCO and NCCO significantly improved when cycled at 2.0–3.7 V. The result suggests the P′3–O3′ phase transition at 4.0 V causes the capacity fading for both the NCO and NCCO. Another phase transition at 2.7 V also affects the cycling performance of NCO. The NCO electrode cycled within the P′3 single-phase region: 2.8–3.7 V shows excellent capacity retention of >80% even after 200 cycles. The XRD study of the cycled electrodes reveals the deterioration process of the NCO. The NCO electrodes form Co_3O_4 during the cycling tests. The amount of the Co_3O_4 formed during the cycling test corresponds to the capacity loss. The P′3–O3′ phase transition at 4.0 V is the most significant capacity fading process because the cobalt ions easily migrate into the sodium vacancies to form the Co_3O_4. The Ca-substituted sample effectively suppresses the formation of Co_3O_4 because the electrostatic repulsion between the substituted Ca^{2+} ion and the $Co^{3+/4+}$ ions probably prevents the migration of $Co^{3+/4+}$ ions into Na layers. The traces of the electrolyte decomposition process detected in the ATR-FTIR spectra suggest that the oxidation of the solvent molecules or anion species compensates the oxidation state of the cobalt ions and accelerates the migration into the Na layer. The Ca-substitution studies in the present work will contribute to the material design strategies to suppress the transition metal migration of Na_xTMO_2.

Acknowledgments

This work was partially supported by Element Strategy Initiative of MEXT, Grant Number JPMXP0112101003, KAKENHI of MEXT, Grant Number 19H05813 and KAKENHI of JSPS, Grant Number 18K19131. The computation was carried out using the computer resource offered under the category of General Projects by Research Institute for Information Technology, Kyushu University.

ORCID

Minoru Mizuhata https://orcid.org/0000-0002-4496-2215
Hideshi Maki https://orcid.org/0000-0002-8960-4833
Masaki Matsui https://orcid.org/0000-0003-1499-7457

References

1. N. Yabuuchi, K. Kubota, M. Dahbi, and S. Komaba, *Chem. Rev.*, **114**, 11636 (2014).
2. C. Delmas, C. Fouassier, and P. Hagenmuller, *Physica B*, **99**, 81 (1980).
3. N. Yabuuchi, H. Yoshida, and S. Komaba, *Electrochemistry*, **80**, 716 (2012).
4. D. Susanto, M. K. Cho, G. Ali, J.-Y. Kim, H. J. Chang, H.-S. Kim, K.-W. Nam, and K. Y. Chung, *Chem. Mater.*, **31**, 3644 (2019).
5. C. Delmas, J.-J. Braconnier, C. Fouassier, and P. Hagenmuller, *Solid State Ionics*, **3–4**, 165 (1981).
6. Y. Lei, X. Li, L. Liu, and G. Ceder, *Chem. Mater.*, **26**, 5288 (2014).
7. M. Guignard, C. Didier, J. Darriet, P. Bordet, E. Elkaïm, and C. Delmas, *Nat. Mater.*, **12**, 74 (2013).
8. K. Kubota, I. Ikeuchi, T. Nakayama, C. Takei, N. Yabuuchi, H. Shiiba, M. Nakayama, and S. Komaba, *The Journal of Physical Chemistry C*, **119**, 166 (2015).
9. A. Mendiboure, C. Delmas, and P. Hagenmuller, *J. Solid State Chem.*, **57**, 323 (1985).
10. J. J. Braconnier, C. Delmas, and P. Hagenmuller, *Mater. Res. Bull.*, **17**, 993 (1982).
11. H. Yoshida, N. Yabuuchi, and S. Komaba, *Electrochem. Commun.*, **34**, 60 (2013).
12. N. Yabuuchi, M. Kajiyama, J. Iwatate, H. Nishikawa, S. Hitomi, R. Okuyama, R. Usui, Y. Yamada, and S. Komaba, *Nat. Mater.*, **11**, 512 (2012).
13. I. Saadoune, A. Maazaz, M. Ménétrier, and C. Delmas, *J. Solid State Chem.*, **122**, 111 (1996).
14. S. Komaba, N. Yabuuchi, T. Nakayama, A. Ogata, T. Ishikawa, and I. Nakai, *Inorg. Chem.*, **51**, 6211 (2012).
15. N. Yabuuchi, M. Yano, H. Yoshida, S. Kuze, and S. Komaba, *J. Electrochem. Soc.*, **160**, A3131 (2013).
16. M. Matsui, F. Mizukoshi, and N. Imanishi, *J. Power Sources*, **280**, 205 (2015).
17. S. C. Han, H. Lim, J. Jeong, D. Ahn, W. B. Park, K.-S. Sohn, and M. Pyo, *J. Power Sources*, **277**, 9 (2015).
18. Y. Ishado, H. Hasegawa, S. Okada, M. Mizuhata, H. Maki, and M. Matsui, *Chem. Commun.*, **56**, 8107 (2020).
19. L. Q. Sun et al., *Small*, **14**, 1704523 (2018).
20. L. Zheng, J. C. Bennett, and M. N. Obrovac, *J. Electrochem. Soc.*, **166**, A2058 (2019).
21. F. Izumi and K. Momma, *Solid State Phenomena*, **130**, 15 (2007).
22. G. Kresse and J. Furthmüller, *Comput. Mater. Sci.*, **6**, 15 (1996).
23. G. Kresse and J. Furthmüller, *Physical Review B*, **54**, 11169 (1996).
24. J. L. Kaufman and A. Van der Ven, *Phys. Rev. Mater.*, **3**, 015402 (2019).
25. G. Henkelman and H. Jónsson, *J. Chem. Phys.*, **113**, 9978 (2000).
26. G. Henkelman, B. P. Uberuaga, and H. Jónsson, *J. Chem. Phys.*, **113**, 9901 (2000).
27. D. Morgan, A. Van der Ven, and G. Ceder, *Electrochem. Solid-State Lett.*, **7**, A30 (2004).